

## Research Article

# Influence of Spatially Varying Flow on the Dynamic Response of a Waterjet inside an SES

Michael R. Motley,<sup>1</sup> Brant R. Savander,<sup>2</sup> and Yin L. Young<sup>3</sup>

<sup>1</sup>Department of Civil and Environmental Engineering, University of Washington, Seattle, WA 98195, USA

<sup>2</sup>Maritime Research Associates, LLC, Ann Arbor, MI 48104, USA

<sup>3</sup>Department of Naval Architecture and Marine Engineering, University of Michigan, Ann Arbor, MI 48109, USA

Correspondence should be addressed to Michael R. Motley; [mrmotley@uw.edu](mailto:mrmotley@uw.edu)

Received 30 April 2014; Accepted 13 October 2014; Published 3 December 2014

Academic Editor: Farid Bakir

Copyright © 2014 Michael R. Motley et al. This is an open access article distributed under the Creative Commons Attribution License, which permits unrestricted use, distribution, and reproduction in any medium, provided the original work is properly cited.

Surface Effect Ships (SES) are a promising fuel-efficient ship technology that typically carry most of their weight on an air cushion. To accommodate its shallow draft and slender side hulls and to absorb the high thrust and power required for high-speed applications, waterjets are typically used as the primary propulsion system. A waterjet typically has a flush mounted inlet and operates under complex three-dimensional flow conditions that result in highly nonuniform flows. The objectives of this work are to quantify the flow nonuniformity and the influence of unsteady cavitation on the response of an SES-waterjet system and to investigate the effect of flow nonuniformity and cavitation on the dynamic hydroelastic response of the rotor and stator blades. The results showed that as the flow advances through the pump, the ingested boundary layer from the bottom of the side hulls becomes increasingly nonuniform, particularly between the rotor and stator. The flow nonuniformity was shown to result in hydrodynamic load fluctuations and high side forces on the rotor and stator blades. The unbalanced blade loads lead to the generation of net upward forces on the pump casing and shaft. Flow nonuniformity also leads to unsteady cavitation and unsteady blade stresses and deformations.

## 1. Introduction

The Surface Effect Ship (SES) is a promising fuel-efficient advanced ship technology that typically carries approximately 80% of its weight on an air cushion. The pressurized air is trapped by two rigid side hulls as well as flexible bow and stern seals. By lifting most of the vessel above the water, the wetted area and hence frictional resistance are drastically reduced at high speeds.

To accommodate the shallow draft and slender side hulls of an SES and to absorb the high thrust and power required for high-speed applications, waterjets are typically used as the primary propulsion system. In addition, waterjets offer good maneuverability at all speeds via the use of a steerable nozzle to create vectored thrust.

Although waterjets offer many advantages, the low draft of an SES and interactions with the air cushion may lead to problematic air ingestion, especially when operating in

high sea states. Other design trade-offs include reduced efficiency at low forward speeds (caused by increased wetted surface area and higher rotational speeds) and at off-design conditions (e.g., near the hump speed).

The design of a waterjet propulsion system is also more complex than for a conventional open propeller. A waterjet propulsion system typically has a flush mounted inlet and operates under complex three-dimensional (3D), unsteady, highly nonuniform flow conditions, including vortical structures and innate unsteadiness [1]. The complexity of the inflow is caused by ingestion of the hull boundary layer at the inlet, the adverse pressure gradient and flow separation inside the S-shaped pump casing, the blockage caused by the presence of the impeller shaft, the effect of shaft rotation, and the effect of impeller-stator interaction [2].

Waterjet propulsion for SESs is even more complicated because of inflow variations associated with interrelated effects of vessel motion, flexible seals, air cushion dynamics,

and waves generated within the air cushion space and around the side hulls. The influence of flow nonuniformity may lead to performance decay and early cavitation inception, which can cause thrust breakdown, blade vibration, and elevated noise levels, particularly for heavily loaded applications. As the amount of vapor in the system increases, supercavitation begins to form on the suction side of the blades where the cavity length reaches or exceeds the blade trailing edge, which limits the pressure on the suction side to be vapor pressure and drastically reduces the pressure on the pressure side as the pressure at the foil's trailing edge must be equal to the vapor pressure. Consequently, the load, or net pressure difference, drops significantly; that is, thrust and torque breakdown develops. If cavitation progresses sufficiently, the pump will reach choke conditions, where almost all of the fluid in the pump system is vapor, thus reducing or eradicating the effective flow area. At this point, practically no thrust or torque occurs [1].

Inflow variations also have the potential to generate high-pressure pulses and large lateral loads on the pump casing and shaft. Moreover, the shallow draft and large air cushion of SES can cause air suction into the waterjet when operating in high seas, leading to a significant degradation in thrust and torque. The large load fluctuations can lead to blade and/or shaft vibrations, accelerate fatigue of the gears and prime movers, and may even cause engine shutdown and affect vessel maneuverability. Hence, it is important to understand and be able to predict the impact of SES-waterjet interactions and flow nonuniformity on the pump performance.

The objectives of this work are (1) to quantify the level of flow nonuniformity and the influence of unsteady cavitation on the mean and unsteady response of an SES-waterjet system and (2) to investigate the effect of flow nonuniformity and cavitation on the dynamic hydroelastic response of the rotor and stator blades.

*1.1. Simulation of Waterjet Performance.* Most previous waterjet simulations applied either inviscid or quasisteady (axisymmetric) CFD assumptions. An excellent review of the mechanics, design, and analysis of waterjets can be found in works by Allison [3] and Allison and Liang [4], which focused on the application of momentum and lifting surface theory for pump performance calculations. Taylor et al. [5] introduced a coupled lifting-surface and RANS approach for computing the quasisteady interactions between the impeller, stator, and duct for the analysis and design of waterjet pumps. The predicted head rise and torque compared reasonably well with experimental measurements presented in Taylor and Kimball [6] and Kimball et al. [7], but there were noticeable deviations due to the inability of the method to capture viscous losses in the rotor region. More recently, investigation of the quasisteady cavitating performance of waterjet propulsion systems includes the work of Sun and Kinnas [8], using a 3D potential-based method coupled with a 2D boundary layer solver, as well as Kim et al. [9], using 3D multiphase RANS solvers. Chesnakas et al. [10, 11] ran model-scale experimental tests at the NSWCCD facility on the AxWJ-2 pump by placing the pump inside a 36-inch cavitation tunnel and observed the flow conditions with Laser

Doppler Velocimetry (LDV). In addition to measuring the thrust and power at different flow rates and tunnel pressures, pressure was also measured at every significant point along the pump. The numerical simulations in [10, 11] used only one rotor blade and one stator blade in calculations because of assumed periodic behavior. Lindau et al. [1] used the same experimental data as Chesnakas et al. [10, 11] but applied a powering iteration approach to simulating the flow through the AxWJ-2 pump. Periodic conditions are assumed for the rotor and stator, but the influence of flow nonuniformity through the duct is captured using a 3D RANS solver. Good comparisons were shown between numerical predictions and experimental measurements, including locations of thrust breakdown. The authors [1] attributed the thrust breakdown to choking caused by excessive vapor fraction near the blade tip.

The aforementioned numerical methods all assume periodic conditions for the stator and rotor and hence are only valid for spatially uniform inflow. It is well known that the flow through the waterjet is highly nonuniform due to the 3D geometry and the ingested boundary layer and interactions between the inlet, duct, impeller, stator, and nozzle. According to Verbeek and Bulten [12], approximately 7–9% of the total power is lost due to flow separation and nonuniformity at the intake duct.

The influence of flow nonuniformity on waterjet performance has been the subject of several recent studies. Bulten and van Esch [13] presented a fully transient CFD analysis for two waterjet pumps, with both three- and six-bladed impellers, to investigate the effect of flow nonuniformity on rotor-stator interactions and the resulting unsteady forces acting on the impeller blades and shaft. They found that flow nonuniformity had negligible influence on rotor-stator interactions, but it leads to the generation of a steady radial force acting on the impeller shaft, which was later confirmed via experimental studies inside a cavitation tunnel [14]. If not properly accounted for, the high radial force can lead to excessive wear of bearings and seals, pump casing vibrations, noise, and early fatigue [14]. A similar transient CFD analysis of stator-rotor interaction inside a waterjet pump was presented by Gao et al. [15]. It was found that the presence of the stator helped to improve the pump efficiency by reducing energy loss due to swirl, and that the efficiency improvement decreases with increasing distance between the rotor and the stator.

*1.2. Waterjet-Hull Interactions.* The effect of waterjet-hull interaction is dominated by boundary layer ingestion on the inflow wake, as discussed by the ITTC [16, 17]. Consequently, quantification of the flow nonuniformity is necessary to determine the proper wake fraction and thrust deduction factors used in the design of waterjets, and for the matching of the waterjet to the vessel thrust and power requirements. However, it is difficult to experimentally quantify the inflow wake and its impact on pump performance due to challenges with measuring the capture area, scaling issues associated with differences in Reynolds number on Froude-scaled models, and difficulties in measuring detailed pump performance for self-propelled tests [16, 18].

In ITTC [17], a waterjet system test was recommended to quantify the effect of waterjet-hull interaction and flow nonuniformity on pump performance. An example of a waterjet system test can be found in Guo and Chen [19]. They reported that the level of nonuniformity is only weakly dependent on the inlet geometry and instead is strongly correlated with the inlet velocity ratio.

In addition to a waterjet system test, a self-propulsion test may also be used to investigate the effect of waterjet-hull interactions. Jessup et al. [18] performed systematic model-scale measurements of the flow field and vessel resistance with and without waterjet propulsors, as well as detailed flow field measurements at various stations along the pump, for the Joint High Speed Ship (JHSS) hull form with three different transom shapes. They demonstrated that the flow through the pump is highly nonuniform and quantified the level of flow nonuniformity via momentum and energy nonuniformity factors. They reported a significant variation in the thrust deduction factor (approximately 25% in low speeds and approximately 5% in high speeds), primarily due to difficulty in scaling the inlet wake, which has a significant impact on the delivered horsepower.

In addition to experimental challenges, it is also difficult to numerically simulate the effects of waterjet-hull interactions. In Hino and Ohashi [20], a steady-state RANS analysis was performed to investigate the free surface flow around a waterjet-propelled displacement hull with fixed trim and draft. The effect of the waterjet was considered using an actuator disk model inside the duct. The results showed noticeable differences in the computed wave patterns and hull surface pressures between the cases with a towed bare hull, a towed hull with duct, and a self-propelled hull with duct and an actuator disk. Stern et al. [21] presented CFD analysis of a waterjet self-propelled high-speed trimaran in both calm water and irregular seas. Validation of the CFD predictions of the waterjet performance for the JHSS was presented by Kandasamy et al. [22]. More recently, Kandasamy et al. [23] introduced an integral force and moment waterjet model for CFD analysis and power predictions of a high-speed semiplaning hull by considering the effects of shaft loading induced by the waterjet and its impact on the vessel sinkage and trim.

It should be noted that none of the above-mentioned experimental and numerical studies of waterjet-hull interactions concern SESs. Only a few open publications related to SES-waterjet interactions exist, the majority of which focus on field test data of model-scale or full-scale vessels with limited detail on data collection. Steen [24] presented both model-scale and full-scale waterjet performance data for the Fast Patrol Boat KNM Skjold to demonstrate the sudden drops in torque due to air ingestion in high seas. Air ingestion for SESs in high seas was also mentioned by Ohba et al. [25].

Although full-scale performance of SES with waterjet propulsion systems has been reported in a few articles, the authors are not aware of any open publications of systematic numerical or experimental studies to investigate the effect of flow nonuniformity on SES-waterjet interactions.

Hence, the objective of this work is to investigate the impact of SES-waterjet interactions and flow nonuniformity

on pump performance via fully coupled CFD simulations and resulting impact on the structural response of the rotor and stator blades via one-way coupled fluid-structure interaction simulations.

## 2. Methodology

To model the transient hydrodynamic response of an SES-waterjet system, the commercial computational fluid dynamics (CFD) code STAR-CCM+ is used to solve the incompressible, Unsteady Reynolds Averaged Navier Stokes (URANS) equations governing the flow. Consider

$$\begin{aligned} \frac{\partial p}{\partial t} + \frac{\partial(\rho v_j)}{\partial x_j} &= 0 \\ \frac{\partial(\rho v_i)}{\partial t} + \frac{\partial(\rho v_i v_j)}{\partial x_j} &= -\frac{\partial p}{\partial x_i} + (\mu + \mu_\tau) \frac{\partial}{\partial x_j} \left( \frac{\partial v_i}{\partial x_j} + \frac{\partial v_j}{\partial x_i} - \frac{2}{3} \frac{\partial v_j}{\partial x_j} \right), \end{aligned} \quad (1)$$

where  $v_j$  is the fluid velocity,  $x_j$  is the location of the fluid particle,  $\rho = \gamma\rho_l + (1 - \gamma)\rho_v$  is the fluid density and the subscripts “ $l$ ” and “ $v$ ” refer to the liquid and vapor, respectively,  $\gamma$  is the volume fraction of liquid,  $t$  is time,  $p$  is the pressure,  $\mu = \gamma\mu_l + (1 - \gamma)\mu_v$  is the dynamic viscosity, and  $\mu_\tau$  is the turbulent viscosity. Detailed formulations of the classical URANS are comprehensively discussed and documented in the STAR-CCM+ reference manuals and are not presented here. The volume of fluid (VOF) method is applied to capture the free surface. The SST  $k$ - $\omega$  turbulence model [26] and the Sauer cavitation model [27] are used for the simulations.

For modeling the structural response of the rotor and stator blades, the commercial finite element method (FEM) solver ABAQUS is used to solve the dynamic equation of motion, defined as

$$\mathbf{M}\ddot{\mathbf{u}} + \mathbf{C}\dot{\mathbf{u}} + \mathbf{K}\mathbf{u} = \mathbf{F}, \quad (2)$$

where  $\mathbf{M}$ ,  $\mathbf{C}$ , and  $\mathbf{K}$  are the structural mass, damping, and stiffness matrices, respectively,  $\ddot{\mathbf{u}}$ ,  $\dot{\mathbf{u}}$ , and  $\mathbf{u}$  are the structural acceleration, velocity, and displacement vectors, respectively, and  $\mathbf{F}$  is the nodal force vector induced by the fluid loading computed from STAR/CCM+. Detailed formulation of the solid equation of motion is discussed in the ABAQUS reference manuals and is not presented here. The dynamic hydroelastic analysis is performed using a one-way coupled simulation between STAR-CCM+ and ABAQUS. This is deemed acceptable because the blade deformations are expected to be very small for practical applications. Detailed dynamic time histories of the pressure and wall shear stresses, calculated using STAR-CCM+, are applied on the FEM model as normal and tangential surface tractions on the rotor and stator blades and are defined in the force vector,  $\mathbf{F}$ , as shown in (2). The rotor and stator blades are assumed to be fixed at the hub, and the stator blades are also assumed to be fixed



FIGURE 1: Mesh and geometry of the AxWJ-2 waterjet.

at the pump casing. Additional details about the coupling methodology can be found in the STAR-CCM+ reference manuals.

### 3. Experimental Validation Studies

**3.1. Validation Results.** The waterjet ONR AxWJ-2's geometry and the corresponding mesh are shown in Figure 1. The computational model has the same dimensions as the pump in the Chesnakas experiments noted above [11]. The rotor intake casing is 0.2 m, the hub diameter is 0.038 m, and the diameter at the nozzle exit is 0.14 m. The waterjet has 6 rotor blades and 8 stator blades, and the total computational domain consists of approximately 3.35 million cells, divided among the intake volume (180,000), rotor (1,792,000), and stator (1,378,000).

The model was validated by comparing numerical results for normalized head rise,  $H^*$ , and power,  $P^*$ , as a function of the normalized volumetric flow rate,  $Q^*$ , and cavitation coefficient,  $N^*$ , with the NSWCCD experimental data in steady, uniform inflow. The variables are defined as follows:

$$\begin{aligned} H^* &= \frac{P_{t6} - P_{t3}}{\rho n^2 d^2}, \\ P^* &= \frac{P_d}{\rho n^3 d^5}, \\ Q^* &= \frac{Q_j}{n d^3}, \\ N^* &= \frac{g * NPSH}{n^2 d^2}, \end{aligned} \quad (3)$$

where  $Q_j$  is the volumetric flow rate,  $P_d$  is the power,  $n$  is the rotor rotational frequency,  $d$  is the diameter of the case at the rotor entrance,  $NPSH = (p_{t3} - p_v)/\rho g$  is the net pressure suction head,  $p_v$  is the vapor pressure of water, and  $p_{t3}$  and  $p_{t6}$

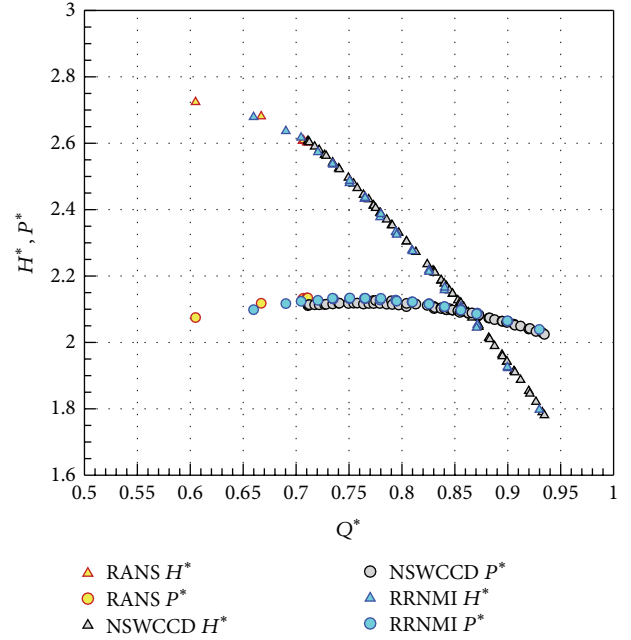


FIGURE 2: Fully wetted RANS predictions compared to experimental measurements inside cavitation tunnels at NSWCCD and RRNMI.

correspond to the pressures at the rotor entrance and nozzle exit, respectively.

Cavitating flow is modeled by initializing the simulation with a fully wetted flow condition; then the cavitation model is turned on and simulations are run until the solution converges. As shown in Figure 2, the predicted (RANS) wetted head rise and power matched well with the experimental measurements conducted at the Naval Surface Warfare Center, Carderock Division (NSWCCD) and at Rolls Royce Naval Marine, Inc. (RRNMI). Details about the experimental setup and results can be found in [10, 11]. The cavitating results, shown in Figures 3 and 4, normalized by their fully wetted counterparts,  $H_o$  and  $P_o$ , followed the general trend of cavitation breakdown curve from the NSWCCD experimental data, and the location of the thrust breakdown, where  $H^*$  begins to drop due to massive cavitation, is well-predicted. Deviations can be observed in the postbreakdown portion, which is most likely due to the difficulty in maintaining a constant flow rate once massive cavitation develops, as noted by [1, 9–11]. Figure 5 also shows good matching between the predicted and observed cavitation patterns [10, 11] on the rotor blade.

Validation of the SES without the waterjet with model-scale measurements was shown in [28]. The objective here is to investigate the influence of flow nonuniformity on full-scale SES-waterjet systems, the details of which are provided herein.

### 4. Full-Scale Simulation of an SES-Waterjet System

**4.1. Problem Setup.** The SES-waterjet system analyzed herein is based on the full-scale, self-propelled ONR T-Craft fitted

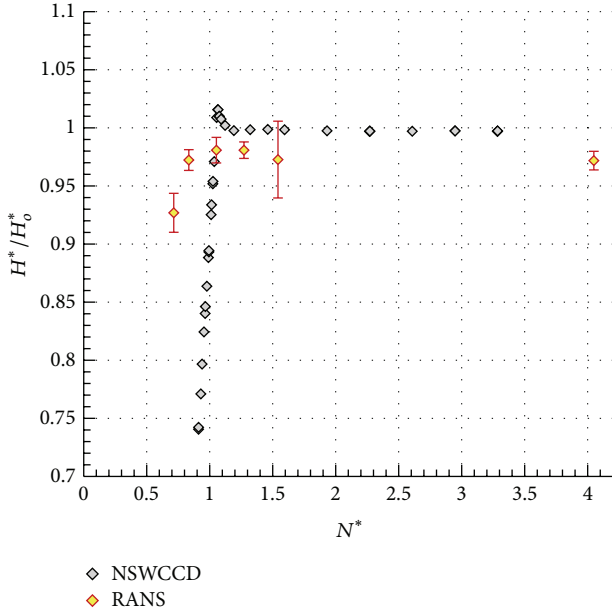


FIGURE 3: Cavitating RANS predictions ( $H^*$ ) compared to experimental measurements at NSWCCD. Note: error bar  $\pm$  represents standard deviation ( $\sigma$ ) of the  $H^*$  time series.

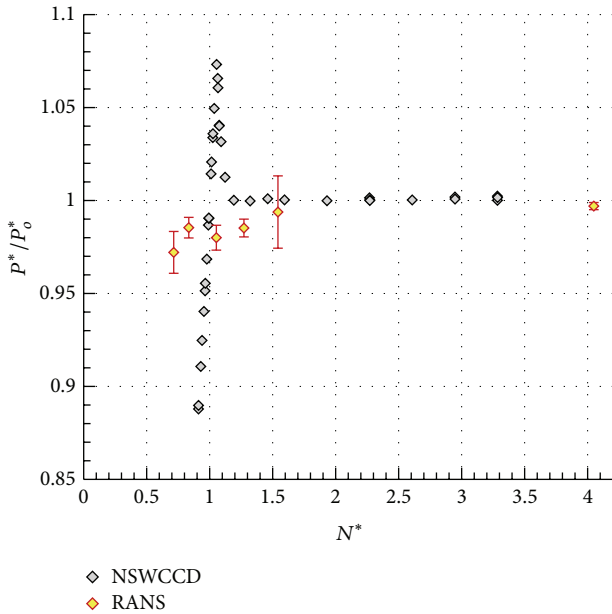


FIGURE 4: Cavitating RANS predictions ( $P^*$ ) compared to experimental measurements at NSWCCD. Note: error bar  $\pm$  represents standard deviation ( $\sigma$ ) of the  $P^*$  time series.

with two AxWJ-2 waterjets [29, 30] and powered by two General Electric LM2500 turbines (one per shaft). Full-scale vessel characteristics of the T-Craft are shown in the right column of Table 1. To overcome the full-scale resistance at the top speed, waterjet-hull matching required the size of the full-scale rotor diameter to be 1.7 m, as shown in Table 2. The geometry of the inlet duct housing is similar to that of

TABLE 1: Full-scale and model-scale vessel characteristics of ONR T-Craft.

| Parameter                | Model-scale | Full-scale |
|--------------------------|-------------|------------|
| Overall length           | 2.53 m      | 76.35 m    |
| Maximum beam             | 0.74 m      | 22.25 m    |
| Cushion length           | 2.22 m      | 67.14 m    |
| Cushion beam             | 0.55 m      | 16.50 m    |
| Percent cushion pressure | 70%         | 70%        |
| Length-to-beam ratio     | 4.0         | 4.0        |
| Displacement             | 55.1 kg     | 1588.6 t   |

TABLE 2: Full-scale and model-scale characteristics of AxWJ-2.

| Parameter        | Model-scale |        | Full-scale |        |
|------------------|-------------|--------|------------|--------|
|                  | Rotor       | Stator | Rotor      | Stator |
| Diameter         | 0.1995 m    | 0.2 m  | 1.6972 m   | 1.7 m  |
| Number of blades | 6           | 8      | 6          | 8      |
| Gap size         | 0.0005 m    | 0.0 m  | 0.00425 m  | 0.0 m  |
| Nozzle diameter  | 0.14 m      |        | 1.19 m     |        |

commercially available waterjet systems. The CFD model of the full-scale SES-waterjet system is shown in Figure 6.

The objective of this work is to investigate the effect of flow nonuniformity on the hydrodynamic and hydroelastic performance of the SES-waterjet system with focus on highly-loaded operating conditions. Hence, only one forward speed,  $V_S = 30$  knots, is considered, corresponding to a cushion length-based Froude number of  $F_r = V_S / \sqrt{gL_c} = 0.6$ , where a validation study with model-scale measurements in bare hull conditions has been presented by Young et al. [28]. The trim and draft position of the SES was determined from steady resistance calculations at 30 knots with the waterjet inlets closed.

The full URANS computational domain and the trimmed hexahedral surface mesh on the T-Craft hullform are shown in Figure 7. Only half of the SES-waterjet system is simulated to take advantage of symmetry in steady, forward conditions for the vessel. Even though the SES is assumed to be in steady-state conditions, the inflow to the waterjet is spatially nonuniform because of the boundary layer flow, which leads to unsteady flow through the waterjet, which is the focus of this work. Velocity inlets are defined on the upstream, top, and bottom boundaries while symmetry conditions are applied on the side and centerline surfaces. A pressure outlet is applied at the downstream boundary. No slip conditions are applied on all solid surfaces.

The surface mesh for the rotor and stator volumes is shown in Figure 8. These domains are constructed from unstructured polyhedron grids. While the tank and stator computational domains are stationary, the rotor computational domain rotates relative to the other two volumes. The tank computational domain communicates with the stator and the rotor domains via nonconformal interfaces located at the nozzle exit and the entrance to the duct inlet, respectively, and the flow solutions are interpolated onto each shared volume face.

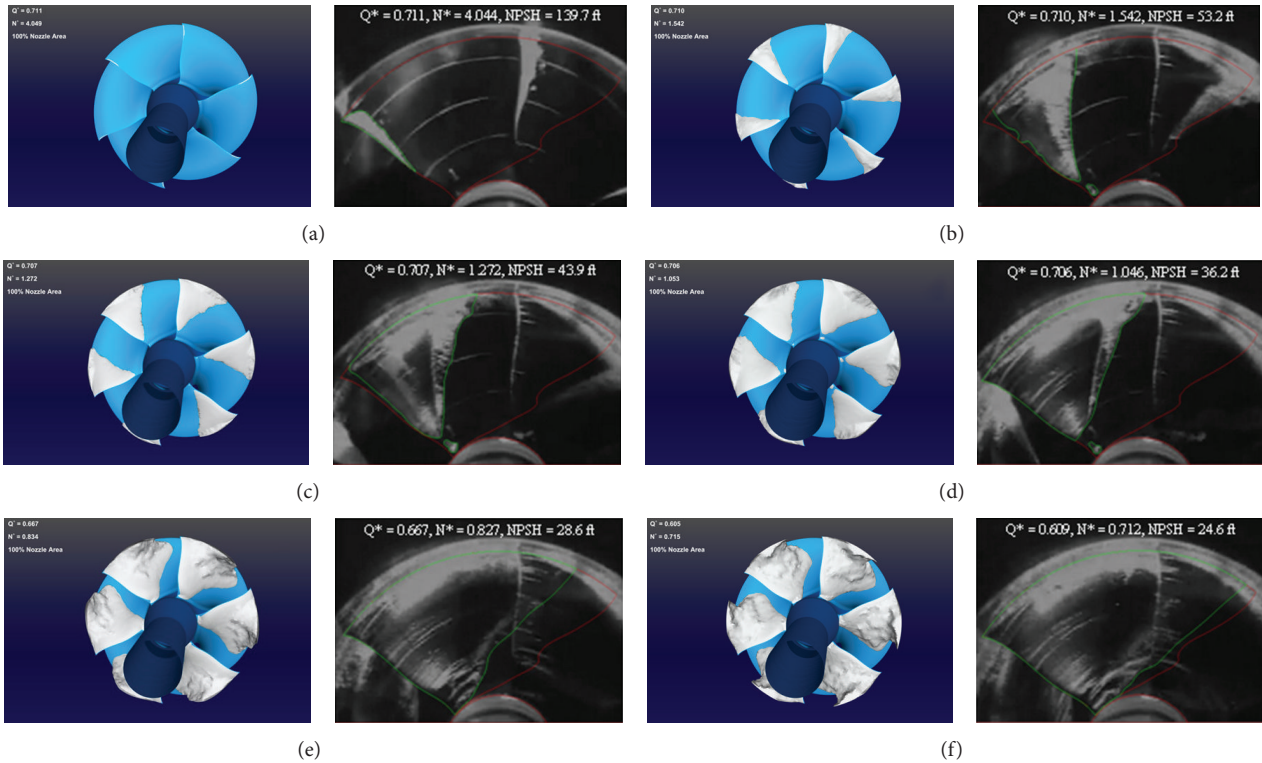


FIGURE 5: Predicted and observed cavitation patterns on the rotor blade (observed results obtained from [10, 11]). (a)  $Q^* = 0.711$ ,  $N^* = 4.044$ ,  $NPSH = 139.7$  ft; (b)  $Q^* = 0.710$ ,  $N^* = 1.542$ ,  $NPSH = 53.2$  ft; (c)  $Q^* = 0.707$ ,  $N^* = 1.272$ ,  $NPSH = 43.9$  ft; (d)  $Q^* = 0.706$ ,  $N^* = 1.046$ ,  $NPSH = 36.2$  ft; (e)  $Q^* = 0.667$ ,  $N^* = 0.827$ ,  $NPSH = 28.6$  ft; (f)  $Q^* = 0.609$ ,  $N^* = 0.712$ ,  $NPSH = 24.6$  ft.

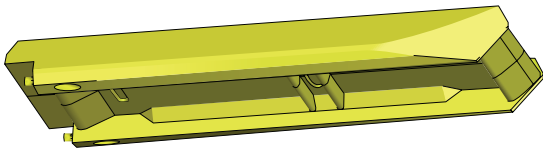


FIGURE 6: Geometric model of ONR T-Craft propelled by two AxWJ-2 waterjets.

The total CFD domain consists of approximately 3 million cells, divided among the tank (676,000 cells), rotor (822,000 cells), and stator (1,522,000 cells). No-slip conditions are applied on all solid boundaries. A time step of 0.001 seconds is used throughout the simulation. Boundary layer prisms are defined along surfaces such that wall values of  $y^+$  are within the range  $10 < y^+ < 50$ .

The computational sequence was to first allow the free surface to stabilize, which was achieved with a large time step size that corresponded to a rotor angular displacement of approximately 15 degrees. Once the free surface was established, the time step size was decreased such that the rotor angular displacement was in the range of 2-3 degrees. The final step in the computational process was to adjust rotor rotational speed such that waterjet thrust was equal to vessel resistance. For the 30-knot case, the equilibrium rotor speed was found to be  $n = 440$  rpm.

## 5. Flow Nonuniformity and Susceptibility to Cavitation

Axial velocity contours and corresponding tangential velocity vectors at several station locations in the waterjet system are shown in Figure 9. Station locations are defined per the 2005 ITTC definitions for waterjet systems [17] and are shown in the top left of Figure 9. The stations of interest are the waterjet inlet (Station-1), rotor inlet (Station-3), rotor outlet/stator inlet (Station-4), stator outlet (Station-5), and nozzle exit (Station-6).

In general, the axial velocity contours are similar to those shown in [18] for axial flow waterjets inside a monohull. At the waterjet inlet (Station-1), the flow is accelerating into the waterjet duct with a maximum normalized velocity,  $V_X/V_S$ , of approximately 1.2, and shows the 3D nature of the inflow resulting from the ingested boundary layer and the inlet geometry. As the flow continues through the duct into the rotor inlet at Station-3, significant spatial variation is shown due to flow nonuniformity at Station-1, the 3D geometry of the pump, and interactions with the six rotor blades and the rotating shaft, which introduced notable tangential velocity to the flow field. A low velocity region is observed at the bottom because of flow deceleration over the elbow.

At the rotor outlet (Station-4), the tangential component of the flow is very high resulting from the rotating rotor blades and shaft, and the wake of the six rotor blades is

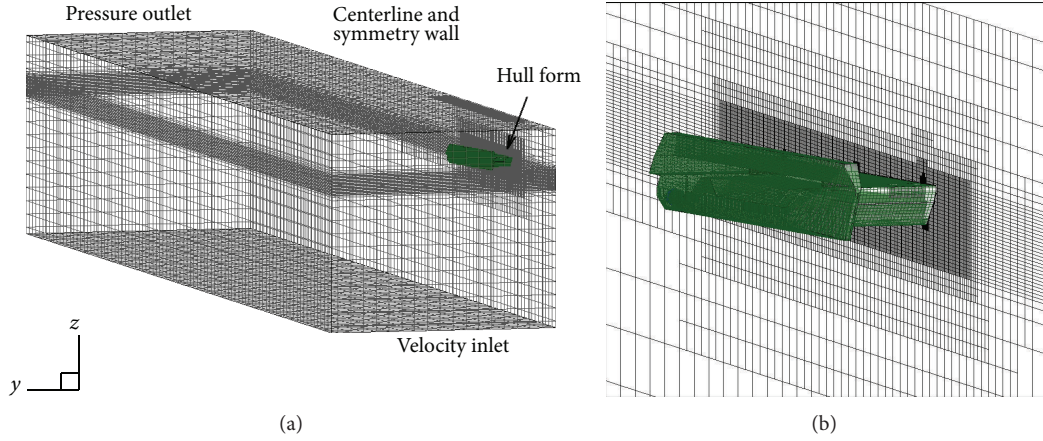


FIGURE 7: URANS computational domain for T-Craft analysis. (a) Full computational domain; (b) closeup view of trimmed hexahedral surface mesh on the hullform.

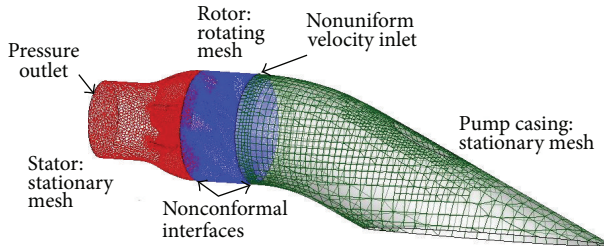


FIGURE 8: Computational domain and polyhedron-based unstructured grid used for waterjet computations.

clearly visible. The maximum normalized axial velocity at Station-4 is approximately 1.5. As the flow passes the 8-bladed stator, most of the swirl energy is recovered, as indicated by the negligible tangential velocity at Station-5. The wakes of the eight stator blades are clearly shown, and the maximum normalized axial velocity is approximately 2.0. Finally, as the flow leaves the nozzle exit (Station-6), the tangential component of the flow is nearly removed, but the axial velocity contour is still not uniform. The jet velocity ratio, defined as the circumferentially averaged axial velocity at the nozzle exit normalized by the vessel speed, is approximately 1.8.

Following [18], flow nonuniformity through the waterjet is quantified using momentum ( $\beta_M$ ) and energy ( $\beta_E$ ) nonuniformity factors, which represent the ratio of the momentum and energy fluxes, respectively, to the averaged axial velocity ( $\bar{V}_n$ ) at Station- $n$ . The averaged axial velocity and nonuniformity factors are defined as

$$\bar{V}_n = \frac{\int_{A_n} \rho V_X dA}{\rho A_n}$$

$$\beta_M = \frac{\int_{A_n} \rho V_X^2 dA}{\bar{V}_n^2 \rho A_n}$$

TABLE 3: Flow nonuniformity factors for stations 3 through 6.

| Station | Momentum, $\beta_M$ |            | Energy, $\beta_E$ |            |
|---------|---------------------|------------|-------------------|------------|
|         | Wetted              | Cavitating | Wetted            | Cavitating |
| 3       | 1.010               | 1.011      | 1.093             | 1.098      |
| 4       | 1.015               | 1.016      | 1.486             | 1.503      |
| 5       | 1.032               | 1.031      | 1.208             | 1.209      |
| 6       | 1.004               | 1.001      | 1.014             | 1.007      |

$$\beta_E = \frac{\int_{A_n} \rho V_X |V|^2 dA}{\bar{V}_n^3 \rho A_n}, \quad (4)$$

where  $A_n$  is the cross-sectional area at Station- $n$ ,  $\rho$  is the fluid density,  $V_X$  is the axial velocity, and  $|V| = \sqrt{V_X^2 + V_Y^2 + V_Z^2}$  is the velocity magnitude. Table 3 shows a comparison of the flow nonuniformity factors at stations 3 through 6 with and without consideration for cavitation. Note that a value of 1.0 represents spatially uniform flow. As the flow advances through the waterjet, the flow nonuniformity factors increase due to rotor-stator interactions. Station-4, just Aft of the rotor, has the highest flow nonuniformity factors. The flow nonuniformity factor recovers to near unity at the nozzle exit. The energy-based flow nonuniformity factors are consistently higher than the momentum-based flow nonuniformity factors, particularly at Station-4, because of the considerable tangential velocity introduced by the rotor blades.

As shown in Table 3, fluid cavitation tends to increase flow nonuniformity and can significantly affect pump performance. Figure 10 shows the contours of the pressure coefficient,  $C_P = (P_{\text{total}} - P_v)/(0.5\rho V_S^2)$ , where  $P_{\text{total}}$  is the total pressure and  $P_v = 3171$  Pa is the vapor pressure of water at 25°C. The velocity streamlines along the center-plane of the waterjet system are also shown. There are four main areas of concern for cavitation: at the waterjet inlet due to the large inlet angle, at the inlet region of the rotating shaft due to the large relative inflow angle, and on the rotor and stator blades

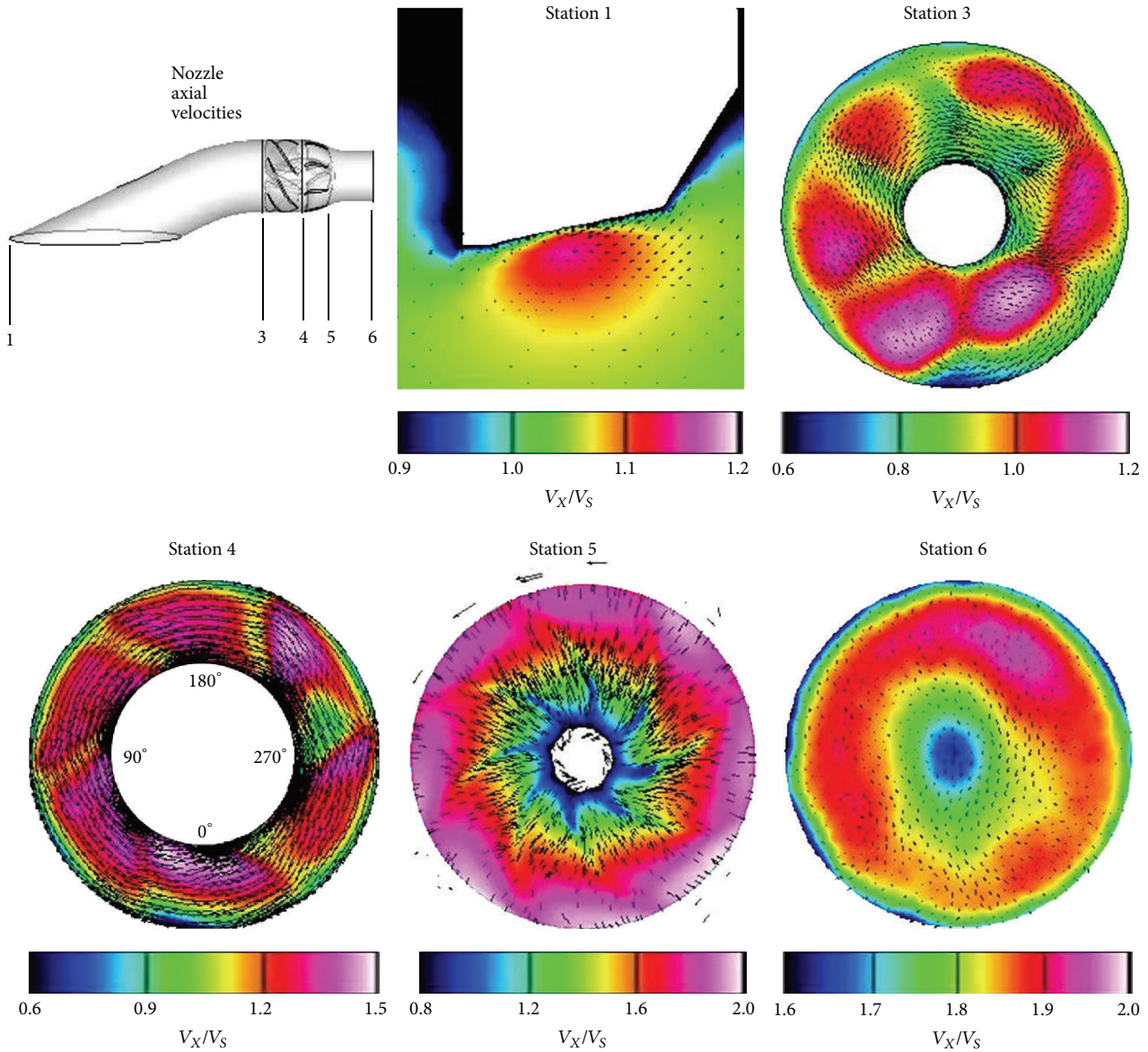


FIGURE 9: ITTC convention for velocity stations for the waterjet (top left, [17]) and axial velocity contours for the case of vessel speed  $V_s = 30$  knots and a rotor speed  $n = 440$  rpm. View from Aft looking upstream. The rotor rotates in the clockwise direction.

due to the high loading condition at  $F_r = 0.6$ , and along the pump casing wall Aft of the stator where the nozzle contracts.

Figure 11 shows the unwrapped normalized pressure distribution and vapor volume fraction on the pump casing wall in the rotor and stator region. The low pressure region, where the nozzle contracts, is cavitating and is clearly visible in Figure 11. The asymmetry in wall pressure that results from the flow nonuniformity can be seen as well. Cavitation is represented by positive values of vapor volume fraction. Regions of cavitation are observed near the tips of the rotor blades, and large-scale cavitation is observed along the entire circumference of the contracting portion of the pump casing region Aft of the stator.

At the waterjet inlet, as shown in Figure 9, the ingested boundary layer flow from the bottom of the side hulls

accelerates into the pump. The high pressure gradient caused by the high inclination angle of the inlet portion of the pump leads to flow separation and cavitation along the lip region, as shown in the vapor volume fraction contours along the pump casing wall looking from the top (left side of Figure 12). The cavitation volume, however, is small, as shown on the vapor volume fraction plot along the center-plane of the pump on the right side of Figure 12, as only a thin cavitation patch is observed at the lip region of the inlet. Again, there is a slight asymmetry to the fluid pressure resulting from the 3D boundary layer flow at the inlet and the axial rotation of the rotor and shaft.

Figure 13 shows vapor volume fraction contours on the shaft, rotor, and stator. A small cavitation patch is shown on the top of the upstream end of the shaft where it connects with

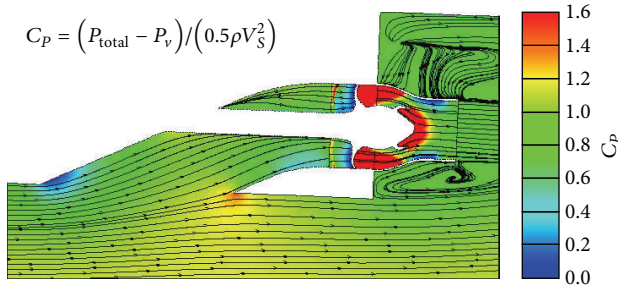


FIGURE 10: Pressure coefficient contours and velocity streamlines across the centerline of the waterjet system.

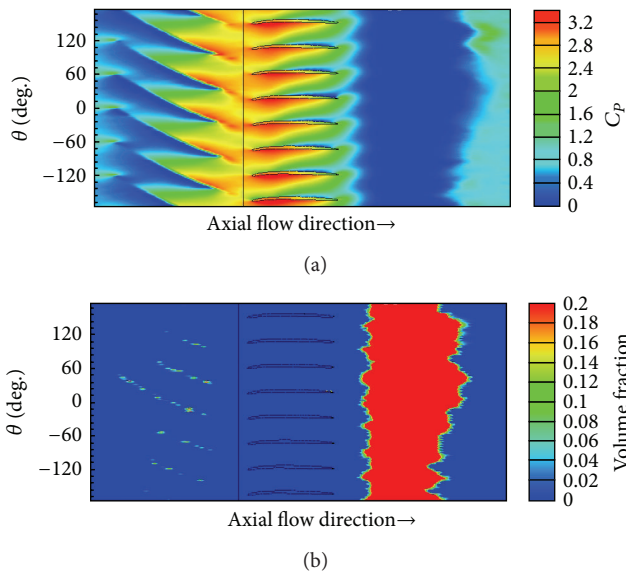


FIGURE 11: Pressure coefficient (a) and volume fraction of vapor (b) contours along the wall pump casing in the rotor, stator, and nozzle region.

the waterjet pump casing and is caused by the high pressure gradient created by the large relative inflow angle. Significant cavitation is observed on the rotor blade surfaces, and some cavitation is observed near the stator blades.

Figure 14 shows the isosurfaces representing 20% vapor volume fraction on both sides of the rotor and stator blades. Thin sheets of unsteady, large-scale cavitation cover the majority of the suction side, and near the trailing edge on the pressure side, of the rotor blades. Unsteady patched cavitation on the suction side and blade root/hub cavitation are also observed on the stator blades. A significant concern of waterjet design is sudden and dramatic thrust/torque breakdown caused by choking where massive cavitation blocks the passing of the flow through the rotor blades. As evident via the isosurfaces shown in Figure 14, the cavitation is relatively thin so choking should not be an issue at this particular combination of vessel speed and rotor rpm. However, additional studies are needed to ensure that choking does not occur at the sub- or primary resistance humps.

## 6. Effects of Flow Nonuniformity and Fluid Cavitation on Dynamic Blade Loads

The flow nonuniformity shown in Figure 9 directly results in time varying forces on the individual components of the waterjet system. Additionally, consideration of fluid cavitation has a significant effect on the estimated forces and resulting pump performance. Figure 15 shows the axial ( $F_x$ ) and radial forces ( $\sqrt{F_y^2 + F_z^2}$ ), normalized by  $0.5\rho V_3^2 D^2$  on a rotor blade as it makes one revolution. Wetted and cavitating results are compared along with the cavitation volume, normalized by the rotor sweep area  $0.25\pi D^2$ , on the blade. The values are shown in the rotating blade-fixed coordinate system. The cavitation volume is maximum between  $250^\circ$  and  $300^\circ$ , corresponding to the low velocity region observed in the lower right hand region in stations 3 and 4 in Figure 9, which is caused by flow deceleration around the bend in the elbow portion of the pump casing. In general, cavitation increases the flow nonuniformity by introducing additional fluctuations and results in slightly higher mean axial and side forces by approximately 1-2%. The mean radial forces on the rotor blades are approximately 80% of the mean axial forces. Fluctuations on the per-blade axial and radial forces are approximately 35% and 30%, respectively, from the mean values.

The left side of Figure 16 shows the normalized per-blade cavitating axial force variation for all six of the rotor blades in their respective rotating blade-fixed coordinate system. While the trends are similar, there is some variability in the axial blade forces resulting from fluid cavitation and flow nonuniformity. Note that blade-1 is highlighted in filled symbols, as it will be used for structural analysis in the following section. The variation of the vertical and horizontal components of the side forces of the 6 rotor blades in the ship-fixed coordinate system is shown on the right side of Figure 16. Although some asymmetry is evident, the net vector sum of the side forces on the rotor is small because the values fluctuate about zero and the variability between the different rotor blade loads is small.

For the stator blades, the amplitude of the per-blade side forces is much larger than that of the axial forces, as shown on the left side of Figure 17. The values are shown in the ship-fixed coordinates since the stator blades are fixed in place. The blade angular positions are in reference to the referenced rotor blade. Six humps are observed on the stator axial and radial forces because of the passing of six rotor blades relative to the fixed stator blade in each revolution. Mean axial forces on the stator blades are approximately 10% of the mean side forces. The effect of flow nonuniformity is evident via the variation of the unsteady blade loads and cavitation volume through the flow cycle. Although cavitation volumes on the stator blades are much less than on the rotor blades, cavitation still leads to an 8.8% increase in the mean axial forces and an approximately 2.7% decrease in the mean radial forces. In addition, the mean radial forces are approximately 12 times higher than the mean axial forces for the stator blades.

The right side of Figure 17 shows the side forces on each of the eight stator blades. Notice that the stator blades are

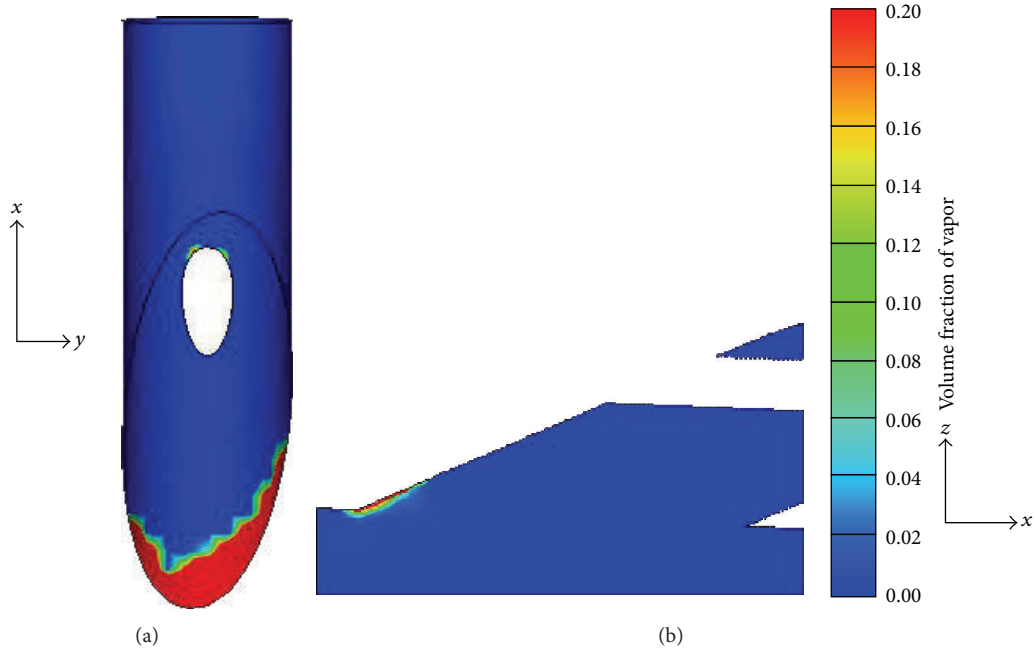


FIGURE 12: (a) Volume fraction of vapor contours showing cavitation at the lip region of the pump casing: view from the top, the oval white region in the middle corresponds to the shaft. (b) Volume fraction of vapor contours along the center-plane of the waterjet, showing cavitation at the lip region of the inlet.

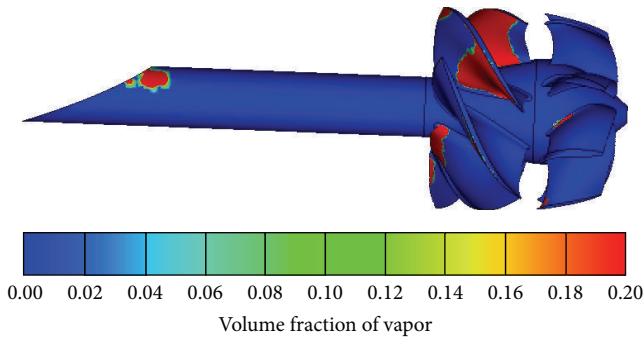


FIGURE 13: Volume fraction of vapor contours on the rotating shaft, rotor, and stator.

fixed and that the scatter of the loading in each stator blade corresponds to the temporal fluctuations in each flow cycle, as demonstrated on the left side of Figure 17. While the magnitude of the side forces is similar for the six rotor blades (Figure 16), the magnitude of the side forces on the eight stator blades varies considerably since they are fixed in place, and they serve to recover the excess swirl energy created by the rotor. The variations in blade loads on the stator will be critical when assessing the structural integrity of the stator blades.

Because the waterjet is a ducted system, flow nonuniformity and fluid cavitation are not the only concerns. In addition, there can be significant thrust loss through frictional resistance along the pump casing and shaft. Figure 18 compares the axial force on the entire pump with the axial

force just from the rotor and stator blades. While the patterns are very similar, approximately 6.5% of the total axial force is lost to the pump casing and shaft, which in part is due to the oversized shaft diameter for the AxWJ-2.

### 7. Resulting Stress Patterns and Deformations

The high level of flow nonuniformity and existence of fluid cavitation lead to dynamic loading conditions on the rotor and stator blades. As shown in Figure 19, the pressure on the blades varies significantly with blade position. As a result, a coupled dynamic analysis is required to determine the structural integrity of the blades.

Using the methodology described in Section 2, structural analyses are performed for the rotor and stator blades using ABAQUS/Standard via time domain analysis. The discretized FEM meshes for the rotor and the stator blades are shown in Figure 20. The rotor and stator are modeled using unstructured, second-order continuum tetrahedral elements and are assumed to be constructed of stainless steel with solid density of  $\rho_s = 7800 \text{ kg/m}^3$ , Young's modulus of  $E = 200 \text{ GPa}$ , Poisson's ratio of  $\nu = 0.3$ , and yield stress of  $\sigma_Y = 450 \text{ MPa}$ . The rotor mesh consists of approximately 58,000 elements while the stator mesh consists of approximately 131,000 elements. Centrifugal and coriolis forces are considered on the rotor blades within ABAQUS by considering the rotational frequency of the rotor ( $n = 440 \text{ rpm}$ ).

Normalized blade deflections and von Mises stress contours of the referenced rotor blade (blade-1 from Figure 16) at several blade angles are shown in Figures 21, 22, and 23. The blade deflections are normalized by the rotor radius,

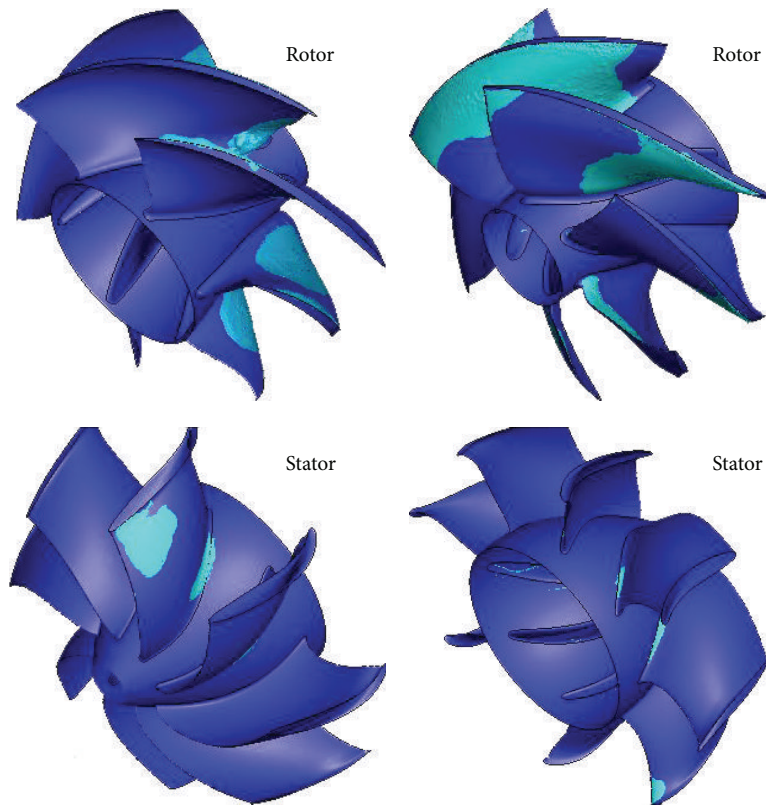


FIGURE 14: Isosurfaces of fluid cavitation volumes corresponding to a volume fraction of vapor of 20% on the rotor and stator blades and hub.

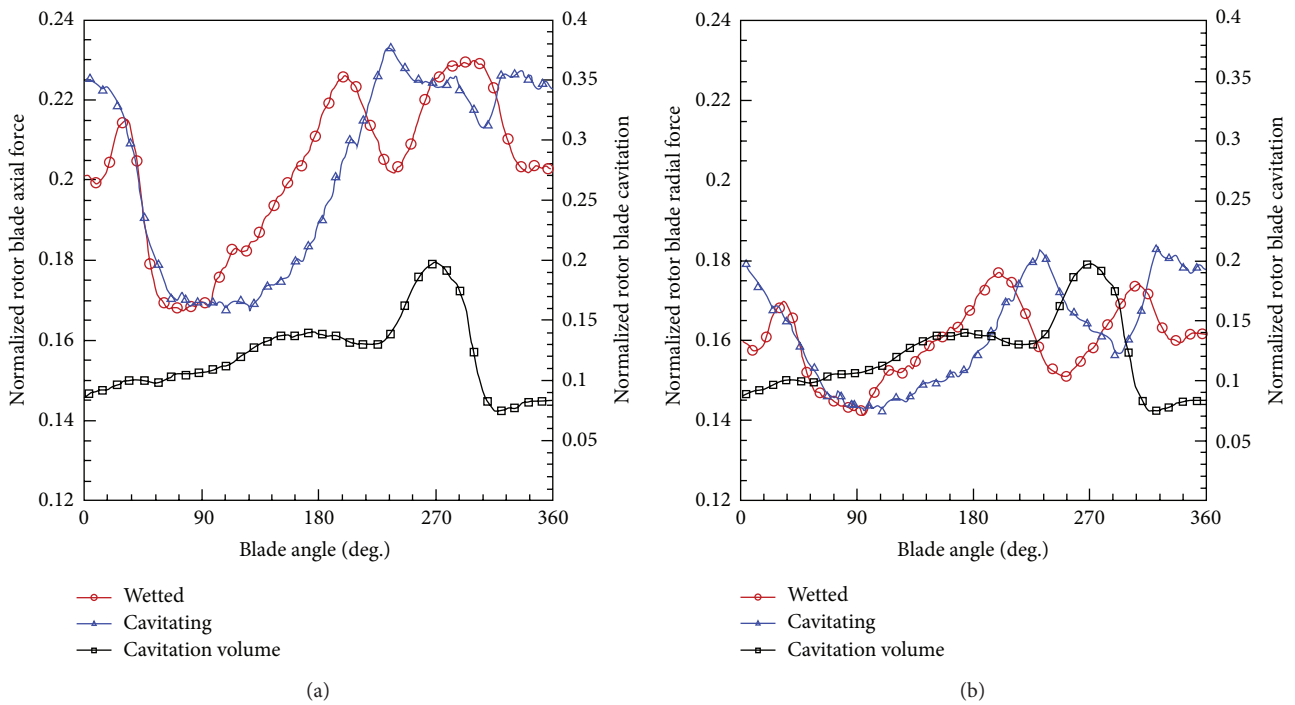


FIGURE 15: Normalized unsteady wetted and cavitating axial forces (a) and radial forces (b), along with the normalized fluid cavitation volume on a rotor blade (blade-1) along one revolution. Rotating blade-fixed coordinate system.

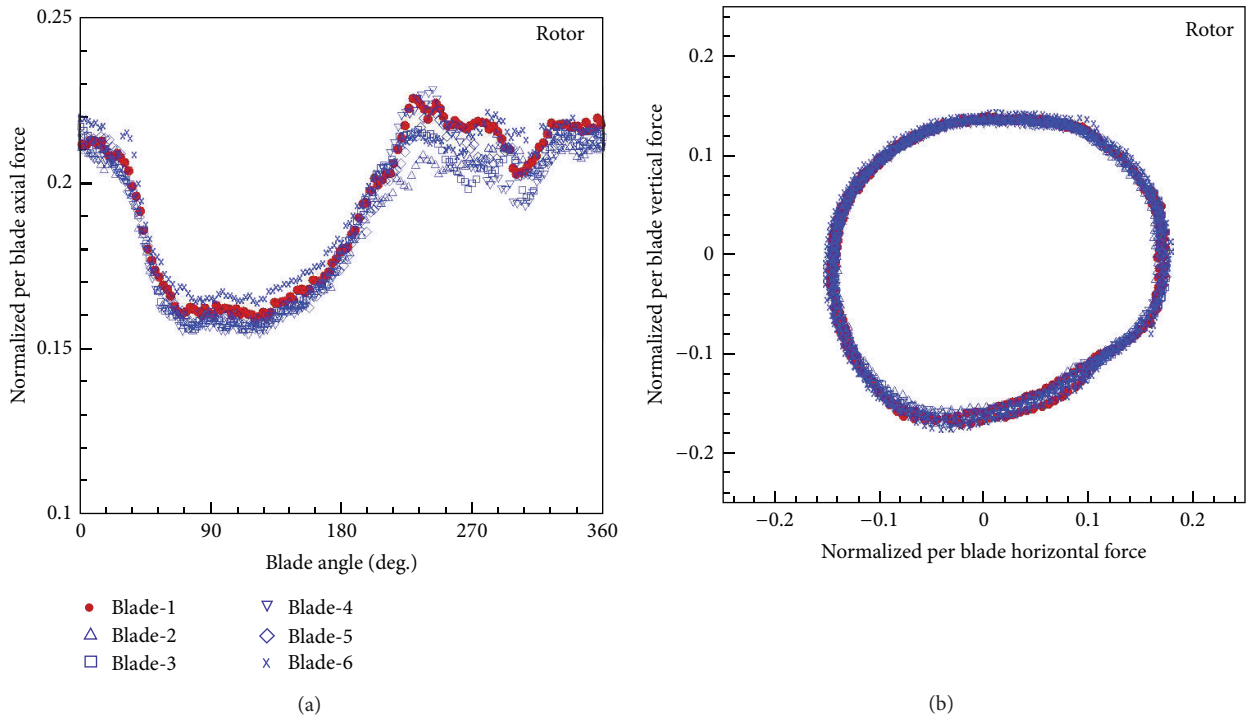


FIGURE 16: Normalized unsteady cavitating axial forces for all six rotor blades along one revolution in rotating blade-fixed coordinates (a), and per blade horizontal and vertical side forces for all six rotor blades in ship-fixed coordinates (b).

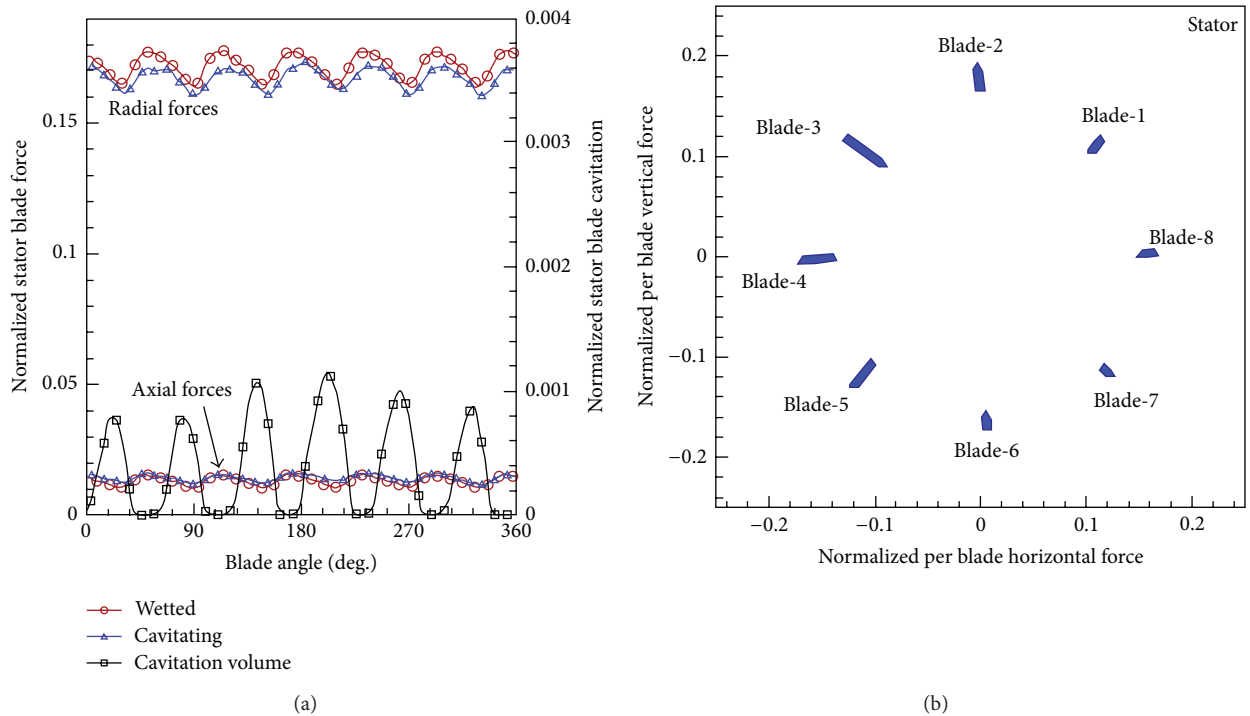


FIGURE 17: Normalized unsteady wetted and cavitating axial forces and radial forces, and the normalized fluid cavitation volume, on a stator blade along one revolution in ship-fixed coordinates with blade angular positions referring to the referenced rotor blade (a) and per blade horizontal and vertical side forces for all eight stator blades in ship-fixed coordinates (b).

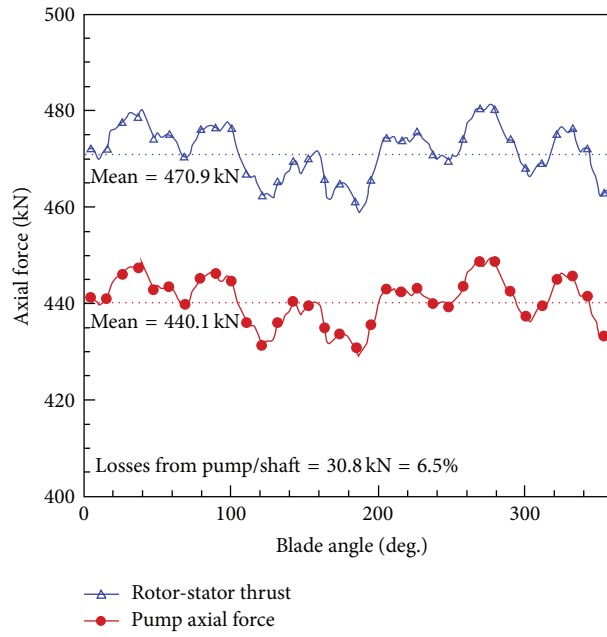


FIGURE 18: Comparison of total axial force on the rotor and stator blades compared to the entire waterjet system.

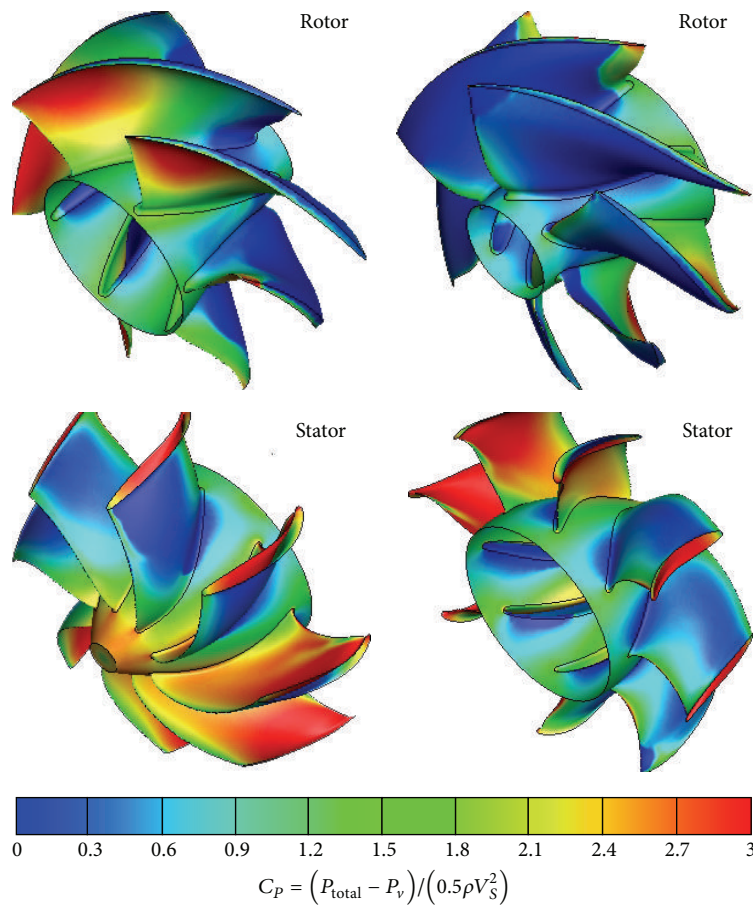


FIGURE 19: Pressure coefficient contours on the rotor and stator blades and hub.

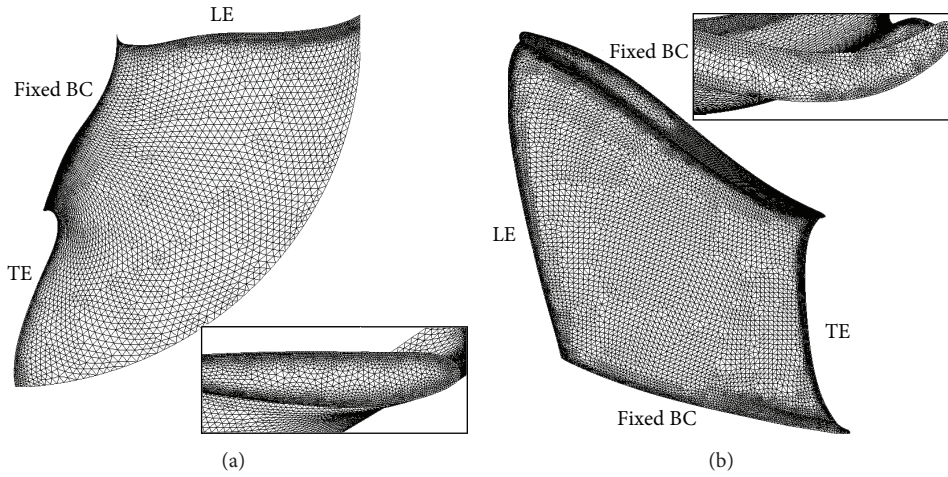


FIGURE 20: Discretized FEM mesh for the rotor (a) and stator (b) blades.

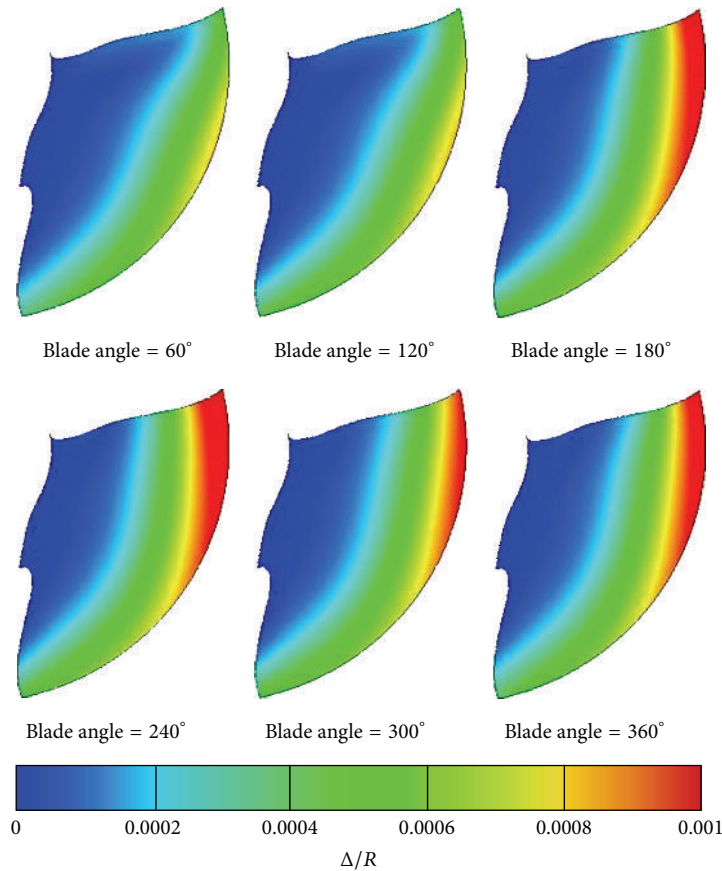


FIGURE 21: Normalized deformation contours for the referenced rotor blade at various blade angles along one revolution ( $R = 0.85$  m).

$R = 0.85$  m. The tip of the rotor blade undergoes small vibrations as it rotates. The maximum normalized tip deflection is approximately 0.16%, or 1.34 mm, which is less than the tip gap clearance of 4.25 mm. The blade deflections are small enough such that their effect on the hydrodynamic response should be negligible, and hence the one-way coupled approach is deemed sufficient. The von Mises stresses are

normalized by the yield strength ( $\sigma_Y = 450$  MPa) of stainless steel. Stress concentrations are observed near the root region on the suction side and near the middle of the blade on the pressure side. The large chord and nonzero pitch and rake distribution of the rotor blades lead to combined bend and twist deformation and hence stress concentrations at the fixed root region. Nevertheless, the maximum normalized stress

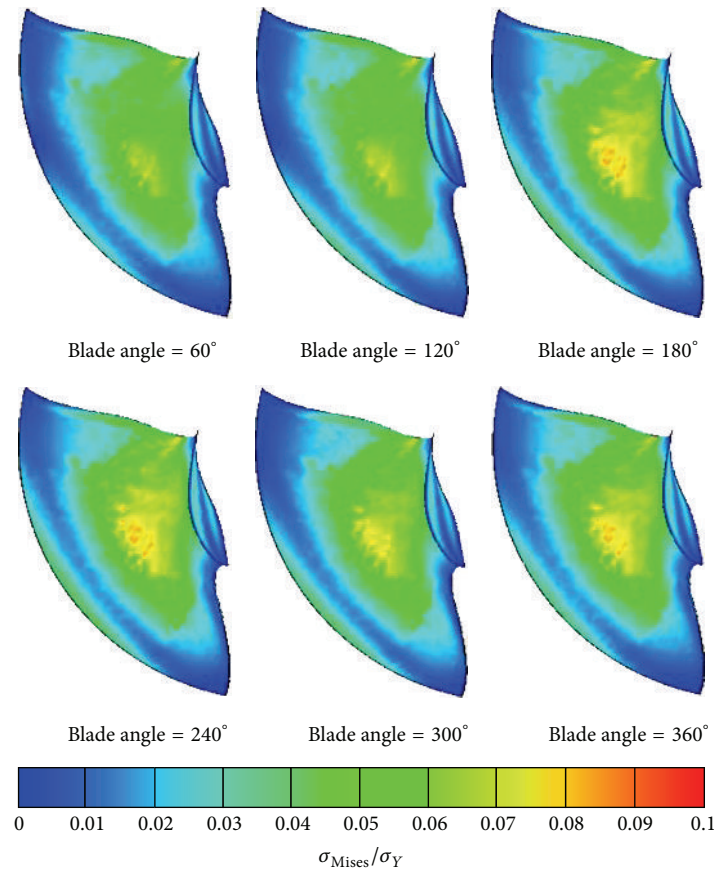


FIGURE 22: Normalized von Mises stress contours on the pressure side of the rotor blade at various blade angles along one revolution ( $\sigma_Y = 450$  MPa).

on the rotor blade shown is approximately 0.15, which is well within acceptable levels.

For the stator blades, analyzing a single blade is not sufficient because of the considerable load variation between the blades. As shown on the right side of Figure 17, the most highly loaded blade is blade-2. The corresponding deformation patterns of blade-2 of the stator at the maximum and minimum loading conditions are shown in Figure 24. Maximum and minimum loads correspond to peaks and valleys, respectively, in the stator loading pattern (Figure 17). A combined bend and twist deformation pattern is observed and is expected given the small moment of inertia against twisting and the fixed boundary conditions at both the tip and the root of the blades. Consequently, stress concentrates near the blade root at the leading edge and near the blade tip at the trailing edge, as shown on the right side of Figure 24. All of the deflections and stresses on the stator blades are well within tolerance, with maximum normalized deflection (by the rotor radius) of 0.008% and maximum normalized von Mises stress (by the yield strength) of 0.15. Hence, one-way coupled fluid-structure interaction simulation is justified, and structural integrity is maintained.

Maximum stress levels noted above are shown relative to the yield stress of the material. Because of the cyclic nature of the loading on the rotor and stator blades, considerations

should be made regarding the fatigue limit of the material. It is not unreasonable to expect a 40–50% decrease in the material strength resulting from fatigue effects; however, the resulting maximum von Mises stresses in the rotor and stator blades, both approximately 15% of the yield stress, would correspond to approximately 25–30% of the fatigue limit of the material, still well within the bounds of structural integrity.

## 8. Conclusions

The objectives of this work are to quantify the level of flow nonuniformity and the influence of unsteady cavitation on the mean and unsteady response of an SES-waterjet system and to investigate the effect of flow nonuniformity and cavitation on the dynamic hydroelastic response of the rotor and stator blades. Failure to properly account for flow nonuniformity and unsteady cavitation can lead to under-conservative estimates of the pump performance and hydroelastic response.

Validation of the CFD predictions with model-scale experimental studies of cavitation tunnel studies of the axial flow waterjet Ax-WJ2 in uniform flow conditions is shown, followed by full-scale simulation of the T-Craft propelled by two Ax-WJ2 waterjets. The results show that, as the flow advances through the waterjet, the ingested boundary layer

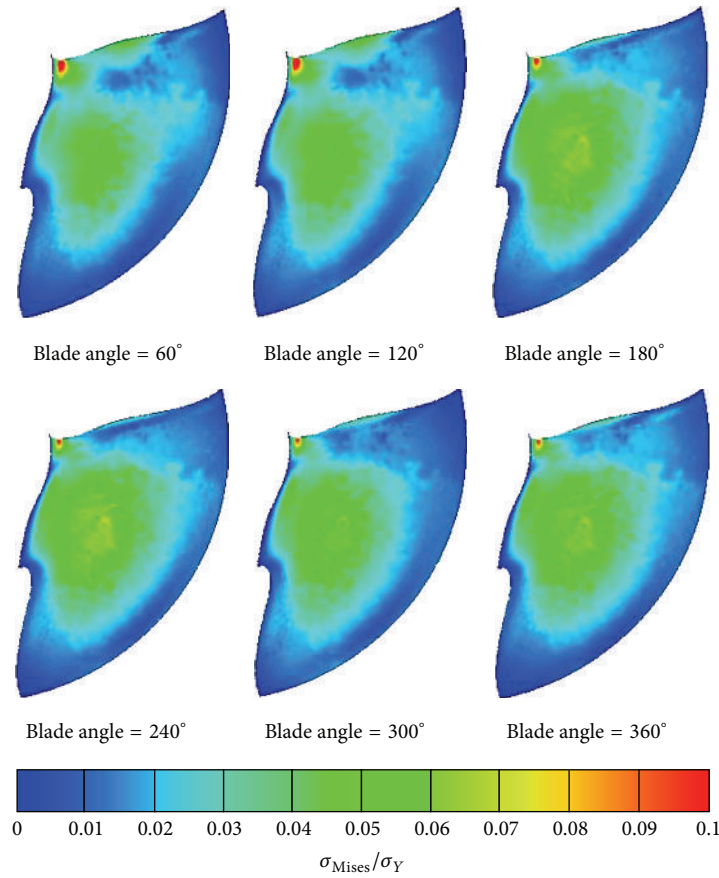


FIGURE 23: Normalized von Mises stress contours on the suction side of the rotor blade at various blade angles along one revolution ( $\sigma_Y = 450$  MPa).

flow from the bottom of the side hull becomes increasingly nonuniform because of the 3D pump geometry and interactions with the rotor and shaft, which leads to unsteady flow conditions for a rotating system. In general, the axial velocity contours along the waterjet are similar to those shown in [18]. The flow nonuniformity factors are found to be the highest at Station-4, just Aft of the rotor, because of 3D pump geometry and the large tangential velocity introduced by the rotor. The energy-based flow nonuniformity factor was found to be consistently higher than the momentum-based flow nonuniformity factor because of the important contribution of the tangential flow velocities. At  $Fr = 0.6$  and a rotor speed of  $n = 440$  rpm, significant cavitation was observed on both the suction and pressure sides of the rotor blades, and some cavitation was observed near the tip and root regions of the stator blades. In addition, cavitation was also observed near the lip region at the inlet, on the top portion of the upstream end of the shaft, and along the contracting portion of the pump casing Aft of the stator. Cavitation leads to increases in the flow nonuniformity factors. Since extensive cavitation was observed because of the high loading conditions, the per-blade axial force increased, the radial force increased on the rotor blades and decreased on the stator blades, and the load fluctuations increased on both the rotor and stator blades compared to the fully wetted condition.

The flow nonuniformity was shown to result in load fluctuations, unsteady cavitation patterns, and high side loads on the rotor and stator components, notably on the stator blades where side forces dominate. The unbalanced blade loads lead to the generation of net upward forces on the pump casing and shaft, which is in agreement with findings presented in [13, 14]. Further, a net loss of 6.5% of the total thrust was shown resulting from the pump casing and shaft. A dynamic hydroelastic analysis was performed on the rotor and stator blades. The maximum deformation of the rotor blades was found to be approximately 0.16% of the rotor radius and approximately 31.5% of the gap size, with a corresponding maximum von Mises stress of approximately 15% of the yield strength. Similarly, the maximum deformation of the stator blade was found to be approximately 0.008% of the stator radius with corresponding maximum von Mises stress of approximately 15% of the yield strength. Thus, it was found that the pump components are within tolerance in terms of both deformation and stress allowance. Similar tolerance was noted for fatigue strength.

The coupled SES-waterjet analysis shown herein was limited to one operating condition, at 30 knots or  $Fr_r = 0.6$  and  $n = 440$  rpm for the full-scale T-Craft operating in steady-state, straight ahead conditions. Further analysis is needed at additional speeds and to consider additional complexity

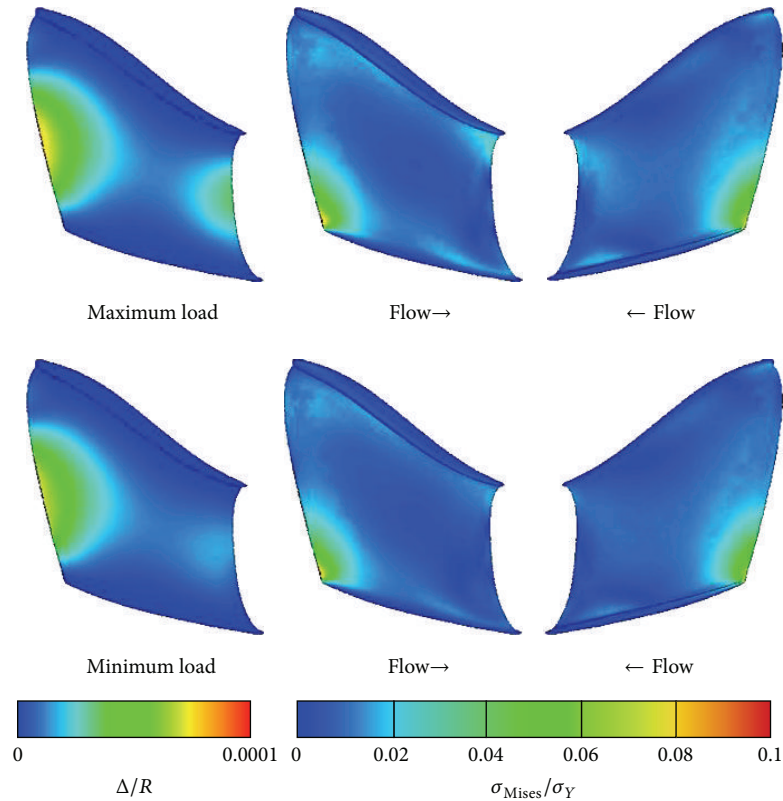


FIGURE 24: Normalized deformation contours (left) and von Mises stress contours (right) for blade-2 of the stator corresponding to the maximum and minimum load experienced by the blade along one revolution ( $R = 0.85$  m,  $\sigma_Y = 450$  MPa).

and flow unsteadiness caused by transient vessel motion and interaction with surface waves. In particular, detailed studies are needed at the sub- and primary resistance humps, which are expected at  $F_r = 0.35$  and  $0.8$ , respectively. Additional systematic convergence and validation studies of the SES only, waterjet only, and coupled SES-waterjet system are also needed. Direct comparisons of the wetted and cavitating performance of the waterjets inside the SES with cavitation pump loop testing across a range of operating conditions will help to further illuminate the effects of flow nonuniformity on the pump performance. Additionally, systematic comparisons of the SES with and without the waterjets across a range of Froude numbers at both the model and full-scale will help to quantify the effects of the waterjets on the SES resistance, as well as to identify scaling effects. Investigations into potential resonance issues for the waterjet system and its components are needed. Exploration of methods to improve the waterjet design (e.g., refine the inlet geometry to avoid lip cavitation, decrease the angle of the elbow to avoid low velocity regions, and refine the contracting part of the pump casing Aft of the stator and of the rotor and stator blades to avoid/minimize cavitation) would provide valuable insights and potential improvements to waterjet performance. Finally, fully coupled simulations of the SES-waterjet system in varying sea states and maneuvers are needed to ensure proper hydrodynamic and structural performance and to avoid inlet broaching issues.

### Conflict of Interests

The authors declare that there is no conflict of interests regarding the publication of this paper.

### Acknowledgments

The authors are grateful to the Office of Naval Research (ONR) and Ms. Kelly Cooper (Program Manager) through Grant nos. N00014-10-1-070 and N00014-11-1-0833 for their financial support.

### References

- [1] J. W. Lindau, C. Pena, W. J. Baker et al., "Modeling of cavitating flow through waterjet propulsors," *International Journal of Rotating Machinery*, vol. 2012, Article ID 716392, 13 pages, 2012.
- [2] P. A. Brandner and G. J. Walker, "An experimental investigation into the performance of a flush water-jet inlet," *Journal of Ship Research*, vol. 51, no. 1, pp. 1–21, 2007.
- [3] J. L. Allison, "Marine waterjet propulsion," *Transactions of the Society of Naval Architects and Marine Engineers*, vol. 101, pp. 273–335, 1993.
- [4] J. L. Allison and C. B. Liang, "Modern tools for water jet pump design and recent advances in the field," in *Proceedings of the International Conference on Waterjet Propulsion: Latest Developments*, Amsterdam, The Netherlands, 1998.

- [5] T. E. Taylor, J. E. Kerwin, and J. O. Scherer, "Waterjet pump design and analysis using a coupled lifting surface and RANS procedure," in *Proceedings of the International Conference on Waterjet Propulsion II*, RINA, Amsterdam, Netherlands, 1998.
- [6] T. E. Taylor and R. W. Kimball, "Experimental validation of a coupled lifting-surface/rans procedure for waterjet pump design and analysis," in *Proceedings of the 5th International Conference on Fast Sea Transportation (FAST '99)*, pp. 893–900, Seattle, Wash, USA, 1999.
- [7] R. W. Kimball, J. O. Scherer, and T. E. Taylor, "Enhancements to the design and analysis of waterjet propulsors using a coupled lifting-surface/RANS technique and comparisons with experiment," in *Proceedings of the International Conference on Waterjet Propulsion III*, Paper no. 9, RINA, Gothenborg, Sweden, 2001.
- [8] H. Sun and S. A. Kinnas, "Performance prediction of cavitating water-jet propulsors," in *Proceedings of the SNAME Maritime Technology Conference & Expo and Ship Production Symposium*, Houston, Tex, USA, 2008.
- [9] S.-E. Kim, S. Schroeder, and H. Jasak, "A multi-phase CFD framework for predicting performance of marine propulsors," in *Proceedings of the 13th International Symposium on Transport Phenomena and Dynamics of Rotating Machinery (ISROMAC-13 '10)*, pp. 7–15, Honolulu, Hawaii, USA, April 2010.
- [10] C. J. Chesnakas, M. J. Donnelly, D. W. Pfitsch, A. J. Becnel, and S. D. Schroeder, "Performance Evaluation of the ONR Axial Waterjet 2 (AxWJ-2)," NSWCCD-50-TR-2009/089, Naval Surface Warfare Center Carderock Division, 2009.
- [11] C. J. Chesnakas, M. J. Donnelly, D. W. Pfitsch, A. J. Becnel, and S. D. Schroeder, "Pump loop testing of an axial flow waterjet," in *Proceedings of the 28th Symposium on Naval Hydrodynamics*, Pasadena, Calif, USA, 2010.
- [12] R. Verbeek and N. W. H. Bulten, "Recent development in waterjet design," in *Proceedings of the International Conference on Waterjet Propulsion II*, RINA, Amsterdam, Netherlands, 1998.
- [13] N. W. H. Bulten and B. P. M. van Esch, "Fully transient CFD analyses of waterjet pumps," *Marine Technology*, vol. 44, no. 3, pp. 185–193, 2007.
- [14] B. P. M. Van Esch, "Performance and radial loading of a mixed-flow pump under non-uniform suction flow," *Journal of Fluids Engineering, Transactions of the ASME*, vol. 131, no. 5, 2009.
- [15] H. Gao, W. Lin, and Z. Du, "Numerical flow and performance analysis of a water-jet axial flow pump," *Ocean Engineering*, vol. 35, no. 16, pp. 1604–1614, 2008.
- [16] ITTC, "The specialist committee on validation of waterjet test procedures: final report and recommendations to the 23rd ITTC," in *Proceedings of the 23rd International Towing Tank Conference*, 2002.
- [17] ITTC, "Testing and extrapolation methods: high speed marine vehicles, waterjets, waterjet system performance, recommended procedures and guidelines," in *Proceedings of the 24th International Towing Tank Conference*, Edinburgh, UK, 2005.
- [18] S. Jessup, M. Donnelly, D. Fry, D. Cusanelli, and M. Wilson, "Performance analysis of a four waterjet propulsion system for a large sealift ship," in *Proceedings of the 27th Symposium on Naval Hydrodynamics*, Seoul, Korea, 2008.
- [19] S. Guo and Y. Chen, "Non-uniform distribution of waterjet inlet flow field," in *Proceedings of the IEEE International Conference on Information and Automation (ICIA '10)*, pp. 1452–1456, Harbin, China, June 2010.
- [20] T. Hino and K. Ohashi, "Numerical simulation of flow around a waterjet propelled ship," in *Proceedings of the 1st International Symposium on Marine Propulsors (SMP '09)*, Trondheim, Norway, 2009.
- [21] F. Stern, P. Carrica, M. Kandasamy et al., "Computational hydrodynamic tools for high-speed sealift," *Transactions of The Society of Naval Architects and Marine Engineers*, vol. 114, pp. 55–81, 2007.
- [22] M. Kandasamy, T. Takai, and F. Stern, "Validation of detailed waterjet simulation using urans for large high-speed sea-lifts," in *Proceedings of the 10th International Conference on Fast Sea Transportation*, Athens, Greece, 2009.
- [23] M. Kandasamy, S. K. Ooi, P. Carrica, and F. Stern, "Integral force/moment waterjet model for CFD simulations," *Journal of Fluids Engineering, Transactions of the ASME*, vol. 132, no. 10, Article ID 101103, 2010.
- [24] S. Steen, "Experiences with seakeeping capabilities of SES ship," in *Proceedings of the RTO AVT Symposium on Habitability of Combat and Transport Vehicles: Noise, Vibration, and Motion*, Prague, Czech Republic, 2004.
- [25] N. Ohba, T. Matsumura, and A. Imakita, "Motion control in waves of a 140M SES," in *Proceedings of the 7th JFPS International Symposium on Fluid Power*, Toyama, Japan, 2008.
- [26] D. Wilcox, *Turbulence Modeling for CFD*, DCW Industries, La Canada, Calif, USA, 2nd edition, 1996.
- [27] J. Sauer, *Instationaer kavitierende Stroemungen-ein neues Modell, basierend auf Fron Capturing VOF und Blasendynamik [Dissertation, thesis]*, Universitaet Karlsruhe, Karlsruhe, Germany, 2000.
- [28] Y. Young, B. Savander, and M. Kramer, "Numerical investigation of the impact of SES-waterjet interactions and flow non-uniformity on pump performance," in *Proceedings of the 11th International Conference on Fast Sea Transportation (FAST '11)*, Honolulu, Hawaii, USA, 2011.
- [29] T. Michael, S. Schroeder, and A. Becnel, "Design of the ONR AxWJ-2 axial flow water jet pump," Tech. Rep. NSWCCD-50-TR-2008/066, Naval Surface Warfare Center Carderock Division, 2008.
- [30] L. Andersson, "ONR AxWJ-2, pump loop test," Tech. Rep. PR-1223, Rolls-Royce Hydrodynamic Research Center, Kristinehamn, Sweden, 2010.

